Article

Influence of Impeller and Mixing Tank Shapes on the Solid–Liquid Mixing Characteristics of Vanadium-Bearing Shale Based on the DEM-VOF Method

Yue Hu [1,2,3], Yimin Zhang [1,2,3,4,*], Nannan Xue [1,2,3,*] and Qiushi Zheng [1,2,3]

[1] School of Resource and Environmental Engineering, Wuhan University of Science and Technology, Wuhan 430081, China
[2] State Environmental Protection Key Laboratory of Mineral Metallurgical Resources Utilization and Pollution Control, Wuhan 430081, China
[3] Hubei Collaborative Innovation Center for High Efficient Utilization of Vanadium Resources, Wuhan 430081, China
[4] Hubei Provincial Engineering Technology Research Center of High Efficient Cleaning Utilization for Shale Vanadium Resource, Wuhan 430081, China
* Correspondence: zym126135@126.com (Y.Z.); xuenannan@wust.edu.cn (N.X.)

Abstract: The mixing tank is important equipment for industrial applications in the wet vanadium extraction process, but in practice, there are problems, such as uneven mixing of minerals. In this study, the effect of different types of impellers and different mixing tank structures on the suspended mass of particles was simulated using the discrete element method and volume of fluid method (DEM-VOF). The simulation results show that the round-bottomed tank performed mixing better than the flat-bottomed tank at different particle densities, and the flat-bottomed tank was prone to particle stratification and other phenomena. The round-bottomed mixing tank could better improve the solid–liquid suspension effect. In this study, the coefficient of variation σ was introduced to characterize the suspended mass of particles. By monitoring the σ value, it was found that the blade pitch angle 45 (BPA45) had the best mixing uniformity in the inclined pitched blade turbine (PBT). As the PBT impeller pitch angle increased, the particle suspension increased. When comparing different types of impellers, the Rushton exhibited a 45% improvement in mixing uniformity relative to the BPA45. Second, the width and height of the trough bottom projection were optimized and their σ values were calculated separately for different parameter conditions. The width of 0.05 m and height T/4 (T being the diameter of the tank) were finally determined to be the optimum parameters for the optimal design of the vanadium shale leaching mixing trough.

Keywords: vanadium shale; mixing tank; computational fluid dynamics; DEM-VOF coupling method

1. Introduction

Mechanical mixing equipment is commonly used in industrial processes, such as power, metallurgy, biology, and food [1–3]. In industrial production, mixing minerals with stirring tanks is an important step in wet extraction [4]. When working, the motor drives the drive shaft to transmit power to the stirring impeller, which makes the stirring impeller perform horizontal, vertical, oblique, and other directions of reciprocating motion, causing the flow field in the stirring tank to have a certain shear force so that the material in the tank can be mixed, stirred, and dissolved. The efficiency of energy transfer directly affects the efficiency of mass and heat transfer in the tank. However, the conventional flat-bottomed stirred tank is prone to particle deposition, stirring dead zones, and uneven mixing [5–7], which affect the dissolution and mineral mixing efficiency, thus reducing the leaching rates of minerals. Scully [8] used computational fluid dynamics (CFD) to study the flow field at the bottom of a flat-bottomed stirring tank and found that the liquid phase velocities near the center and edge of the tank were small and the solid phase concentration

was high, so these two parts were prone to solid phase deposition. The conventional standard 4-baffle has been used to improve solid–liquid mixing, but this structure causes a significant increase in the power of this system and particles tend to accumulate at the baffle, resulting in wear and tear on the equipment. Therefore, it is particularly important to choose an appropriate method for the improvement and optimization of traditional mixing equipment [9].

In recent years, fluid dynamics software has developed rapidly [10] and has been widely used in a wide range of fields, such as equipment development and product design, which significantly saves labor and development costs, and the visualization of simulation results provides more intuitive data for equipment optimization [11–14]. The design of the stirring device has been reoptimized using simulations.

Fluent provides a variety of solid–liquid simulation methods, including discrete phase models (DPMs), denoising diffusion probabilistic models (DDPMs), DEM, etc., each with its own applicable operating conditions. DPM is only applicable for particle volume fractions less than 10%, and it does not take into account the particle volume and particle–particle interaction force. Zhang et al. [15] used the VOF-DPM method to study the wake structure and particle entrainment behavior of bubbles in a solid–liquid system—the particles occupied a relatively small percentage of the simulated system and the particle–particle interaction was negligible. The DDPM [16,17] takes into account collision between particles, and the resulting forces are calculated from the stress tensor of the particles at the kinetic theory of granular flow (KTGF)—this model simplifies the calculation and does not calculate the real collision process.

CFD-DEM is often used to simulate gas–solid or liquid–solid multiphase flows. It allows the direct tracking of particle movements, overcomes the shortcomings of traditional CFD simulation, and can choose more accurate numerical methods to simulate fluid and particles while taking into account particle size, shape, density, and other factors. The VOF model can also be used to simulate the free liquid level of a stirred tank, more closely matching the actual stirring situation. The phases in the Eulerian and mixing models are considered as continuous media running through each other and are often used in simulation processes, such as fluidized beds or pneumatic transport. The VOF model is more suitable for describing the motion of particles in a flow field and their interaction with fluid [18–20]. In this study, the DEM-VOF coupling method is used to study the flow field in a round-bottomed stirring tank and a flat-bottomed stirring tank.

Satjaritanun [21] used a counter-rotating impeller to eliminate vortices and dead zones in the stirring tank, and this structure enhanced the shear pattern of the flow field and intensified the solid–liquid mixing effect, but the mechanical structure of the device was complex, resulting in a highly unstable stirring system. Woziwodzki and Ameur used eccentric stirring [22,23] to improve mixing, but eccentric stirring led to localized mixing inhomogeneity and the stirring impeller was prone to vibration, and was only applicable to small mixing devices. All of the above methods can improve the shortcomings of traditional mixing tanks to some extent, but the mixing system is not easy to maintain. At present, there have been fewer studies on the optimization of mixing tank shape structure. Wu et al. [24] found that an elliptical head mixing tank reduced the generation of a vortex after changing the structure of the mixing tank. Kang et al. [25] found that the shape of the bottom of the mixing tank had a significant effect on the mixing effect. Jia et al. [26] studied a conical-bottomed mixing tank and found that the change in the shape of the tank's bottom accelerated the mixing time and reduced the solid phase deposition; all of the above studies have shown that optimizing the shape of the tank could improve the mixing effect. Therefore, in this paper, the shape of the bottom of the mixing tank was optimized to obtain a better type of flow field to enhance the mixing effect by using the VOF-DEM method through simulation.

2. Mathematical Models

2.1. Coupling Scheme

This study used Fluent 19.0 and EDEM 2018 for coupled simulations. In the simulation calculation, Fluent solved the fluid equation and EDEM solved the particle motion equation. Firstly, Fluent was used to analyze the flow field at a certain moment and the calculated information was then transmitted to EDEM, which was used to analyze the particle condition at this moment. On this basis, EDEM could transmit particle information to Fluent, such as the particle position, temperature, and speed. The interaction between the particle and the liquid was transferred to the EDEM through the interface, the particle was affected by the volume force, and the interaction between the particle and the liquid was a momentum source. When using the coupled model of CFD-DEM, the time step of CFD calculation was limited, the ratio of time step between the two was generally controlled between 10–100 times, and it was an integer multiple.

The calculation process of DEM-VOF model is shown in Figure 1:
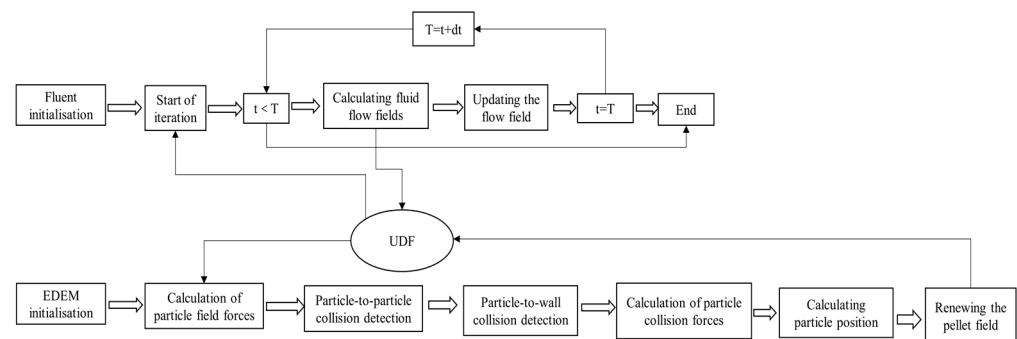
Figure 1. Coupling simulation processes.

2.2. Liquid-Phase VOF Model

VOF model building and tracking were performed under a fixed Euler mesh, on the premise that two or more fluids did not penetrate each other [27]. The VOF model could track the volume fraction of each fluid by solving a set of momentum equations, and the phase interface of each cell was tracked by the phase volume fraction. In each cell, the sum of all phase volume fractions was 1, and all phases shared variables and physical properties.

Thus, depending on the value of the volume fraction, the feature in any cell represented a phase or a mixture of phases and was determined by the number of phase integrals, so three possible cases appeared in the cell [28]:

$\alpha_i = 0$, indicating that the cell was empty;

$\alpha_i = 1$, which meant that the cell was filled;

$0 < \alpha_i < 1$, indicating that the cell contained an interface between the fluid and one or more other fluids.

The dynamic behavior of this interface could be described as:

$$\frac{\partial \alpha_2}{\partial t} + \nabla \cdot (\alpha_2 \boldsymbol{u}) = 0 \tag{1}$$

$$\alpha_1 + \alpha_2 = 1 \tag{2}$$

where α_1 is the primary phase volume fraction, α_2 is the secondary phase volume fraction, and $\boldsymbol{u}$ is the fluid velocity vector.

The transient calculation method was adopted in this paper, so the display time discretization scheme was used to solve the volume fraction equation and the geometric reconstruction method was used to improve the accuracy of the simulation.

In addition, the density and viscosity in the governing equation were calculated in the simulation:

$$\rho = \rho_1\alpha_1 + \rho_2\alpha_2 \tag{3}$$

$$\mu = \mu_1\alpha_1 + \mu_2\alpha_2 \tag{4}$$

The motion continuity equation of the fluid phase is:

$$\frac{\partial \varepsilon_f}{\partial t} + \nabla \cdot \left(\varepsilon_f \boldsymbol{u}\right) = 0 \tag{5}$$

where ρ, μ, and ε_f represent the density, the viscosity, and the void fraction, respectively.

The RSM model is the most detailed RANS turbulence model provided by Fluent. The RSM uses Reynolds [29] stress transport equation and dissipation rate equation instead of the vortex viscosity hypothesis to seal the equation. In this paper, the RSM model was used to solve the equation:

$$\frac{\partial\left(\rho_f\varepsilon_f\boldsymbol{u}\right)}{\partial t} + \nabla \cdot \left(\rho_f\varepsilon_f\boldsymbol{uu}\right) = \varepsilon_f\left(-\nabla p + \nabla \cdot \left(\overline{\tau} - \rho_f\overline{u_i'u_j'}\right) + \boldsymbol{f}_s + \rho_f\boldsymbol{g}\right) + \boldsymbol{f}_{pf} \tag{6}$$

where the fluid density is ρ_f and the fluid velocity is $\boldsymbol{u}$, $\boldsymbol{f}_{pf}$ represents the interaction force between the particle and the fluid, ε_f represents the void fraction, and the expression of the viscous stress tensor τ is:

$$\overline{\tau} = \mu\left((\nabla\boldsymbol{u}) + (\nabla\boldsymbol{u})^T - \frac{2}{3}(\nabla \cdot \boldsymbol{u})\delta_k\right) \tag{7}$$

where the dynamic viscosity is μ, the unit tensor is δ_k, and the Reynolds stress is $\rho_f\overline{u_i'u_j'}$.

$$\boldsymbol{f}_{pf} = \frac{1}{\nabla V}\sum_i^{n_p}\boldsymbol{F}_{p_{f,i}} - \boldsymbol{F}_{\nabla p,i} - \boldsymbol{F}_{\nabla\tau,i} - \boldsymbol{F}_{\nabla\cdot\rho_f\overline{u_i'u_j'},i} - \boldsymbol{F}_{s,i} - \boldsymbol{F}_{s,i} \tag{8}$$

where

$$\boldsymbol{F}_{p_{f,i}} = \boldsymbol{F}_{d,i} + \boldsymbol{F}_{\nabla p,i} + \boldsymbol{F}_{\nabla\tau,i} + \boldsymbol{F}_{\nabla\cdot\rho_f\overline{u_i'u_j'},i} + \boldsymbol{F}_{s,i} + \boldsymbol{F}_{vm,i} + \boldsymbol{F}_{B,i} + \boldsymbol{F}_{Saff,i} + \boldsymbol{F}_{Mag,i} \tag{9}$$

where ∇V is the corresponding mesh cell volume and n_P indicates the particle number. $F_{p_{f,i}}$ represents the total of all interaction forces between particle–fluids, such as drag ($F_{d,i}$), pressure gradient ($F_{\nabla p,i}$), viscous stress force ($F_{\nabla\tau,i}$), Reynolds stress force ($F_{\nabla\cdot\rho_f\overline{u_i'u_j'},i}$), capillary force ($F_{s,i}$), virtual mass ($F_{vm,i}$), Basset force ($F_{B,i}$), Saffman lift ($F_{Saff,i}$), and Magnus lift ($F_{Mag,i}$).

2.3. DEM Model Particle Motion Equation

In the DEM model, the rotational motion of particles is determined by the contact moment, and the transition motion of particles is controlled by the resultant force of particles [30]. The trajectory of particles is calculated as follows[M1]:

$$m_i\frac{d\boldsymbol{v}_i}{dt} = m_i\boldsymbol{g} + \sum_{j=1}^{n_i}\left(\boldsymbol{F}_{n,ij} + \boldsymbol{F}_{t,ij}\right) + \boldsymbol{F}_{pf,i} \tag{10}$$

$$I_i\frac{d\boldsymbol{\omega}_i}{dt} = \sum_{j=1}^{n_i}\left(\boldsymbol{T}_{t,ij} + \boldsymbol{M}_{r,ij}\right) \tag{11}$$

where the total number of particles in the simulation system is n_i, the normal force of particles is $\boldsymbol{F}_{cn,ij}$, the tangential force is $\boldsymbol{F}_{ct,ij}$, the mass is m_i, the inertia moment is I_i, the

velocity is v_i, the angular velocity is ω_i, $F_{c,i}$ is the contact force, and the tangential and rolling friction moments between particles are $T_{t,ij}$ and $M_{r,ij}$.

Among them, the contact force F includes the normal contact force and tangential contact force, expressed as:

$$F_{c,ij} = F_{cn,ij} + F_{ct,ij} = -k_{n,ij}\delta_{n,ij} - \gamma_{n,ij}\dot{\delta}_{n,ij} - k_{t,ij}\delta_{t,ij} - \gamma_{t,ij}\dot{\delta}_{t,ij} \tag{12}$$

where $k_{n,ij}$ and $k_{t,ij}$ are normal and tangential stiffness coefficients, $\gamma_{n,ij}$ and $\gamma_{t,ij}$ are normal and tangential damping coefficients, $\delta_{n,ij}$ and $\delta_{t,ij}$ are the overlaps of normal and tangential particles, and $\dot{\delta}_{n,ij}$ and $\dot{\delta}_{t,ij}$ are the derivatives of $\delta_{n,ij}$ and $\delta_{t,ij}$ with respect to time, respectively.

2.4. Quantitative Standards for Particle Mixing Homogeneity

In order to compare the mixing conditions of particles in the mixing tank under different working conditions, in this study, the coefficient of variation σ was introduced to evaluate the particle suspension's uniformity [31]. The calculation formula of the σ value is 12. If $\sigma > 0.8$, the particle is not completely suspended; if $0.2 < \sigma < 0.8$, the particle is completely suspended from the bottom; and if $\sigma < 0.2$, the particle is in uniform suspension. In this study, the fluid domain was divided into 27 equal-volume regions.

$$\sigma = \sqrt{\frac{1}{n}\sum_{i=1}^{n}\left(\frac{\alpha_{2i}}{\alpha_{2,av}} - 1\right)^2} \tag{13}$$

where n is the total number of samples, α_{2i} is the particle volume fraction of each sample, and $\alpha_{2,av}$ is the average of the particle volume fractions of the 27 samples.

3. Model Validation and Parameters

3.1. Single Particle Falls Free into the Water

In this study, the fluid was in a turbulent state. In order to verify the correctness of the model, the free sedimentation rate of a single particle was simulated under turbulent flow. After falling into the water, the velocity decreased rapidly. When the gravity and buoyancy of the particle reached a balance, the velocity became stable. The specific calculation formula is as follows:

$$u_t = 1.74\sqrt{\frac{d_p\left(\rho_p - \rho_f\right)g}{\rho_f}} \tag{14}$$

$$Re_t = \frac{u_t d_P \rho_f}{\mu_f} \tag{15}$$

The theoretical calculation formula of a single particle in free fall in water is as follows:

$$\frac{\pi}{6}d_P^3\left(\rho_p - \rho_f\right)g - C_D\frac{\pi}{4}d_P^2\left(\frac{\rho_f u_p^2}{2}\right) = \frac{\pi}{6}d_p^3\rho_p\frac{du_P}{dt} \tag{16}$$

In the turbulent region $C_D = 0.44$, u_p is the particle velocity, d_p is the particle diameter, ρ is the density, p is the particle, f is the fluid, u_t is the final velocity of the particle, and μ_f is the viscosity of the fluid.

In this section, three different particle densities were selected as the objects of study, and their simulation conditions in the liquid phase are shown in Table 1. As shown in Figure 2, the comparison with the theoretical results shows that the sedimentation process of solid particles in liquid can be well simulated by VOF-DEM.

Table 1. Parameters of single-particle sedimentation.

Group No.	d_p (m)	ρ_p (kg/m³)	ρ_f (kg/m³)	μ_f (Pa s)	u_t (m/s)	Re_t[27]
(1)	0.002	2400	1078	0.0005	0.2697	1163.21
(2)	0.003	2400	1078	0.001	0.3303	1068.48
(3)	0.004	2400	1078	0.001	0.3815	1645.04
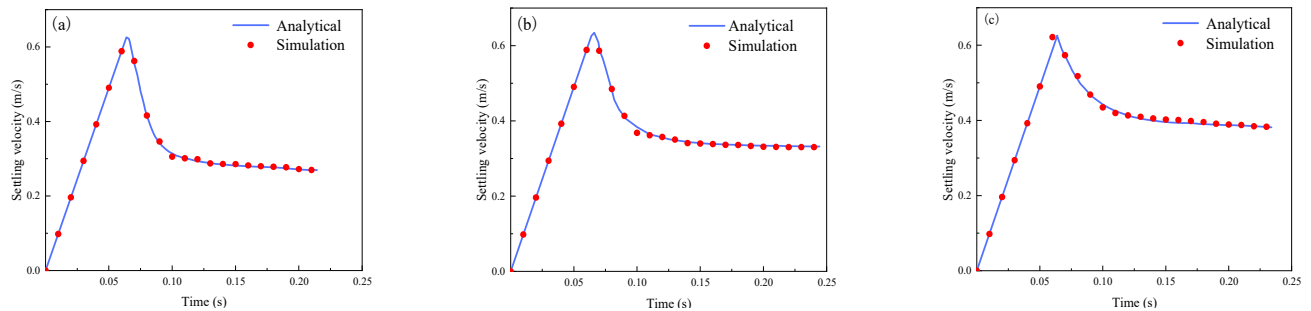
Figure 2. Curve of particle velocity over time: (**a**) group 1; (**b**) group 2; (**c**) group 3.

### 3.2. Model Volume Conservation Verification

The VOF-DEM model considers the volume of particles, so the volume conservation of the model needs to be verified to prove the correctness of the model. The height at which the water level rises when the particles are in a stable state is the volume of all particles divided by the cross-sectional area, this paper uses a 20,480 particle group (ρ = 2400 kg/m³, d = 2 mm) placed at a height of 5 mm from the water; the cross-sectional area of the volume is 2600 mm³. As shown in Figure 3, when all particles had fallen into the water, the calculated water surface height was 32.99 mm according to the theoretical value and the simulated water surface height was 33.85 mm. The error was only 2.60%. The simulation results were compared with the theoretical results, and the results showed that the method was reliable.
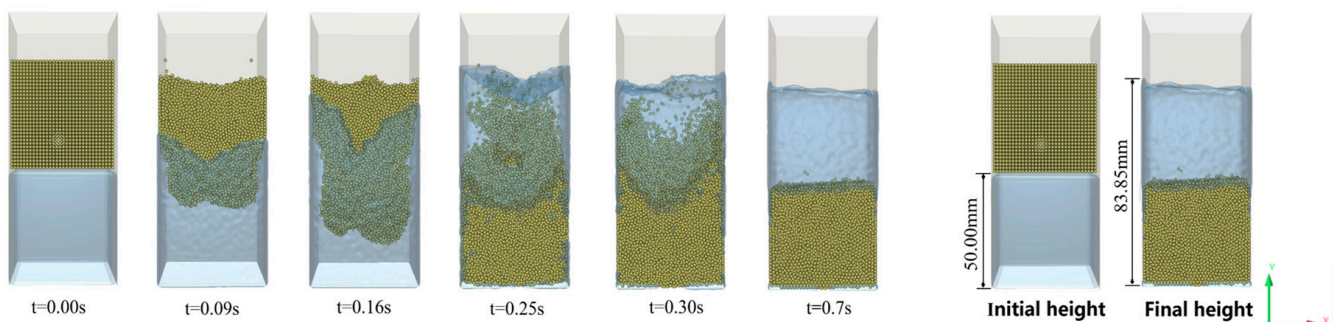
Figure 3. Snapshot of particle swarm settling process in water.

3.3. Grid Independence Verification

The simulation results were highly correlated with the number of grid nodes. Theoretically, the more meshes there are, the closer the simulation results will be to reality. However, the number of meshes should not be too large, because the more meshes there are, the longer the computation time will be, and our computational resources are limited. Therefore, it is necessary to choose the right number of grids for the simulation work in the simulation calculation. In simple terms, grid independence verification actually aims to verify whether the grid is independent of the final calculation results.

The specific method is as follows: first, a larger grid size is selected for the initial simulation calculation, and the simulation results are basically within the acceptable range. Then, the grid size is encrypted and the results of multiple settlements are compared. In this paper, four sets of grid sizes (134 k, 167 k, 218 k, and 385 k) were set, and the solid phase volume fractions under different grid numbers were compared as in Figure 4. With the gradual decrease in the grid size, the difference in the volume fraction became smaller, and when the number of grids reached 385 k, which was almost double the number of grids in the previous set, the change value of the volume fraction was almost the same as 218 k at this time, the maximum difference in the volume fraction was only 2.5%, and the scheme of the 218 k grid number was finally determined.
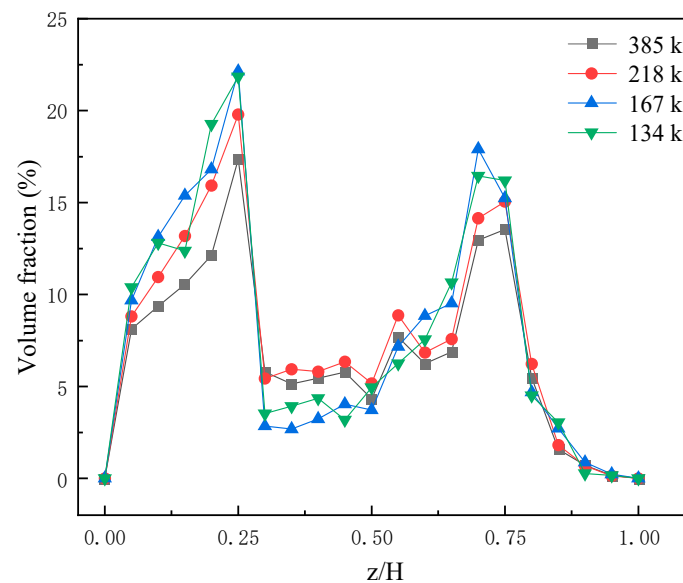

Figure 4. Solid-phase volume fraction distribution curve.

3.4. Geometric Model and Simulation Parameters

This study simulates the object of study with the experimental stirring tank size as a reference, and the specific parameters are shown in Table 2. The optimized elliptical head stirring tank is shown in Figure 5a. Three semi-circular arcs were established at the bottom of the tank and treated symmetrically. The flat-bottomed mixing trough is shown in Figure 5b. The liquid level of the stirring tank is H and its diameter is T.

Table 2. Size of the mixing tank.

Symbol	Items	Geometric Sizes
T	Diameter	0.19 m
H	Liquid level	T
P	Distance between impeller and round bottom	T/8
C	Height	4T/3
L	Diameter of impeller	T/2
E	Ellipsoidal head height	T/6
M	Impeller width	L/5
D	Bump height	T/12, T/6, T/5, T/4, T/3
W	Bump width	0.02 m, 0.03 m, 0.04 m, 0.05 m, 0.06 m, 0.07 m
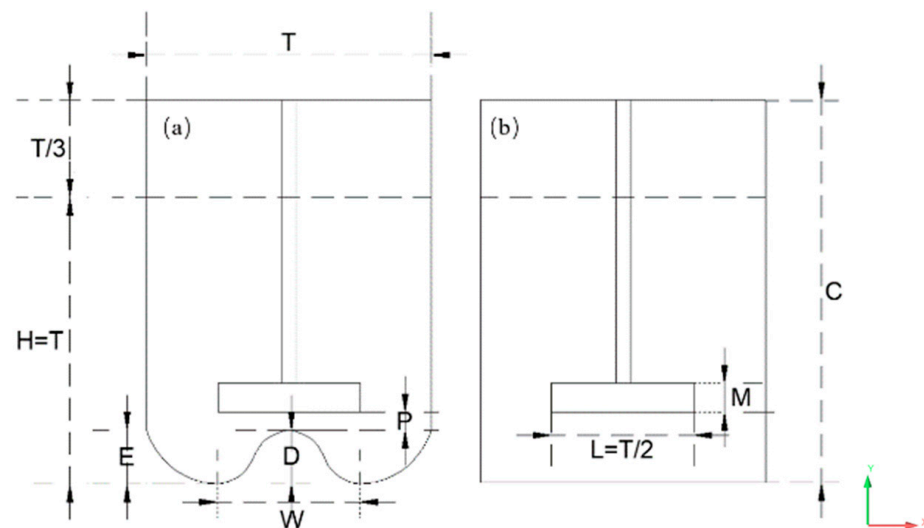
Figure 5. Mixing tank structure diagram: (**a**) round-bottomed agitator; (**b**) flat-bottomed agitator.

4. Results and Discussion

4.1. Influence of Stirred Tank Shape on Particle Suspension and Free Surface

This section investigates the effect of the stirring tank structure on the free liquid level and the uniformity of the particle suspension. A particle size of 2 mm and a quantity of 50,000 particles were selected. The volume fraction of the particles was approximately 4%. The blade type was PBA45 and the speed was 400 rpm. The time step for CFD was 1×10^{-4} s and that for EDEM was 5×10^{-6} s.

The start-up process of the flat-bottomed mixing tank at a particle density of 1200 kg/m^3 is shown in Figure 6a. Clearly, at the beginning (t = 0.4 s), the particles were drawn in by the impeller under the movement of the fluid and, due to the stirring of the impeller, caused the surrounding fluid to flow upward at an incline, with the fluid below carrying the particles to fill the space accordingly and then expel them by the rotation of the paddles. At the same time, the depth of the vortex increased with time until the stability remained essentially constant (t = 4.8 s), at which point the phenomenon of stratification of particles above and below occurred; most of the particles were deposited at the bottom of the trough and a few particles were suspended above the trough. Figure 6b illustrates the start-up process of a round-bottomed stirring tank, where the particles are initially drawn in by the rotation of the blades (t = 0.4 s), similar to the start-up process of a flat-bottomed stirring tank. However, after a certain period of stirring, the particles were not significantly stratified and were uniformly dispersed in the stirring tank by the action of the fluid (t = 4.8 s). The fluid interacted with the particles and no deeper vortices were formed after the round-bottomed stirring tank reached a steady state (t = 4.8 s), indicating that the improved stirring tank could eliminate vortices, to some extent.

Secondly, this section compares the mixing effects of the two mixing tanks at different densities. It is clear from Figure 7 that, at particle densities of 1800 kg/m^3 and 2400 kg/m^3, the particles in the round-bottomed stirring tank reached the upper region of the tank and the particles were better suspended. In contrast, in the flat-bottomed mixing tank, the particles were all deposited at the bottom of the tank as the density increased and the vortex depth decreased as the density increased. The uniformity of the particle suspension in the round-bottomed tanks was low due to the impeller speed.
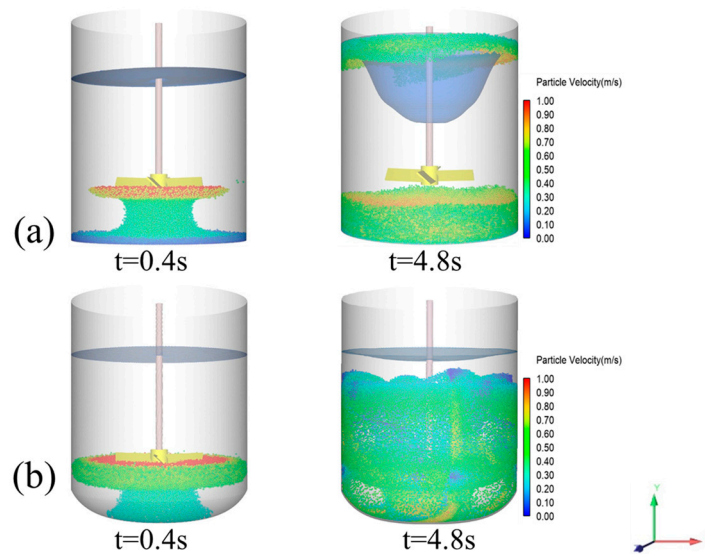
Figure 6. Snapshot of gas–liquid–solid flow in a stirrer, ρ_p = 1200 kg/m^3; (**a**) flat-bottomed agitator, (**b**) round-bottomed agitator.
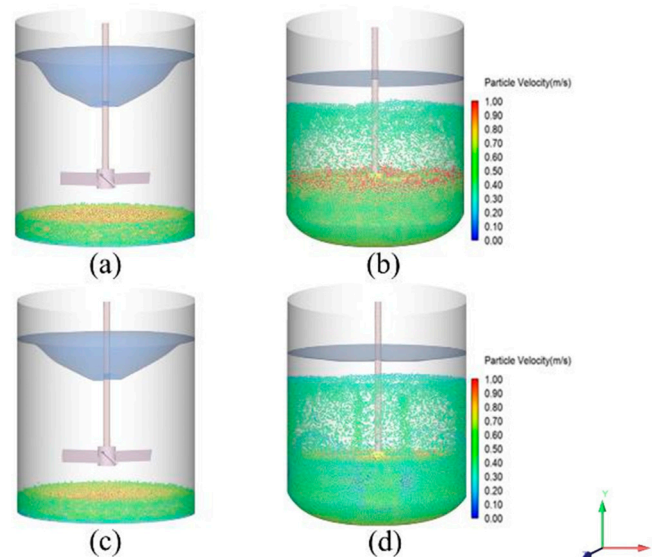

Figure 7. Snapshot of gas–liquid–solid flow in a stirrer, t = 4.8 s; (**a**) flat-bottomed agitator, (**b**) round-bottomed agitator. (**a**,**b**) ρ_p = 1800 kg/m^3 (**c**,**d**) ρ_p = 2400 kg/m^3.

*4.2. The Influence of the Shape of the Stirring Tank on the Flow Field Type*

In order to investigate the stratification phenomenon that occurs in a flat-bottomed stirring tank at a particle density of 1200 kg/m^3, this study explores the type of flow field in the tank. Figure 8 shows the flow pattern of the flow field in the stirring tank. As shown in Figure 8a, in the flat-bottomed stirring tank, when the fluid moved to the tank wall, the velocity of the fluid changed to two vertical velocities, and the particles thrown against the wall moved up and down under the action of the fluid, so the particles showed upper and lower stratification. As the flow field stabilized, the vortex motion of the fluid dominated and eddies began to appear, so the main motion of the particles was vortex motion under the action of centrifugal forces, resulting in a blank area at the center of the bottom (Figure 8c). In contrast, as shown in Figure 8b, in a round-bottomed stirring tank, the flow field formed a circular loop at the bottom of the tank due to the change in the shape of the bottom. This flow pattern decreased the sudden change in fluid velocity at the bottom, decreased the axial velocity of the fluid, had a suppressive effect

on the stratification of the particles, and there was no blank area in the center of the tank (Figure 8d).
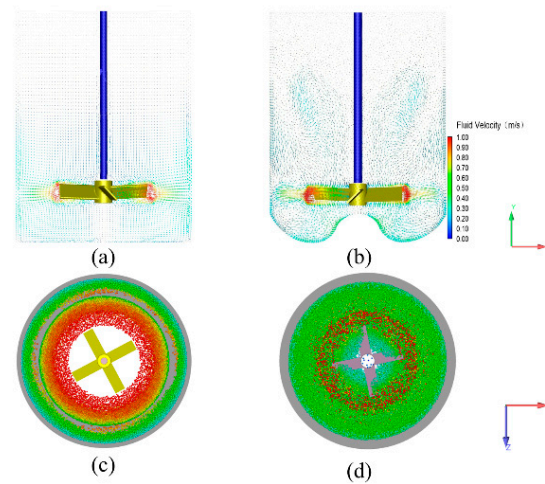
Figure 8. Velocity distribution of the fluid in the mixing tank; (**a**,**c**) flat-bottomed agitator, (**b**,**d**) round-bottomed agitator.

Figure 9 shows two typical particle trajectories in a flat-bottomed stirring tank with a proportion of the particles moving upward through the flow field and the vast majority deposited below the tank in a vortex motion, which is consistent with that depicted in Figure 8 and confirms the stratification of the particles.
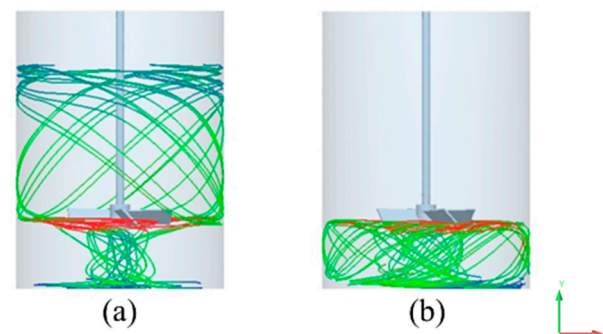
Figure 9. Trajectory of particles in a flat-bottomed mixing tank; (**a**) upward-moving particles, (**b**) downward-moving particles.

4.3. Improvements to the Round Bottom Mixing Tank

4.3.1. Influence of Impeller on Particle Suspension Effect

In order to investigate which paddle blade was the best for stirring in a round-bottomed stirring tank, this part of the simulation was set up with different paddle blades, a PBT and a Rushton blade. The PBT was set at three different inclination angles of 30°, 45°, and 60°. In this part of the simulation, 50,000 particles with a size of 2 mm and a density of 2400 kg/m^3 were selected, and the impeller speed was set at 700 rpm. The particle velocities are distinguished by different colors. The particle suspension effects under different working conditions are shown in Figure 10. As can be seen from these diagrams, when the BPT inclination was greater, the particles could spread more widely, reaching higher regional positions in the mixing tank and eventually reaching the top region of the tank. It can be seen that BPA60 and Rushton had the highest particle suspension heights. However, in the PBA60 mixing tank, although the particles could move to the top of the tank, there was stratification in the mixing tank, which had a certain influence on the particle mixing uniformity. In the PBA30 stirring tank, the particles did not reach the complete suspension state, most of the particles were deposited at the bottom of the mixing tank, and the contact

between the solid phase and liquid phase was not sufficient, which was not conducive to improving the leaching rate. In the BPA45 mixing tank, although only a small number of particles moved to the top of the mixing tank, the particles could be evenly distributed in the mixing tank. In a Rushton mixing tank, there were particles in the upper part of the tank, and the particles were more evenly mixed. However, in some stirring tanks, particles could become suspended in the upper region, but they were likely to move near the tank's wall in response to the centrifugal force of the flow field, so the σ value was chosen to evaluate particle suspension.

The variation in the coefficient of variation σ with time, calculated from the solid volume fraction, is shown in Figure 11. In all stirring tanks, the value of σ fluctuated very violently. After a certain time, the value of σ tended to be stable. At this time, it can be considered to reach a stable state [32]. The σ value of PBA30 converged to 1.6 at 5 s, when the particles had not reached off-bottom suspension. The coefficient of variation σ value for PBA45 was the smallest among the PBTs, at 1.3 under a steady state; this means that the tank was in an incomplete suspension state. The predicted value of PBA60 fluctuated greatly between 1.6 and 0.8, which was due to a certain layering of particles, resulting in large fluctuations in the σ values. The σ value of Rushton remained stable at around 0.6, with better suspension than PBT and an increase in homogeneity of more than 20%. All of the above analyses prove that Rushton had a better suspension capacity.

In the actual production process, we also need to take into account the influence of power; it is important to reduce production costs and power consumption while ensuring adequate suspension of solid particles. The calculation of the mixing power in this simulation is given by

$$P = 2\pi \times M \times \frac{N}{60} \tag{17}$$

where P is the stirring power (W), M is the stirring torque (N-m), and N is the rotational speed (rpm).
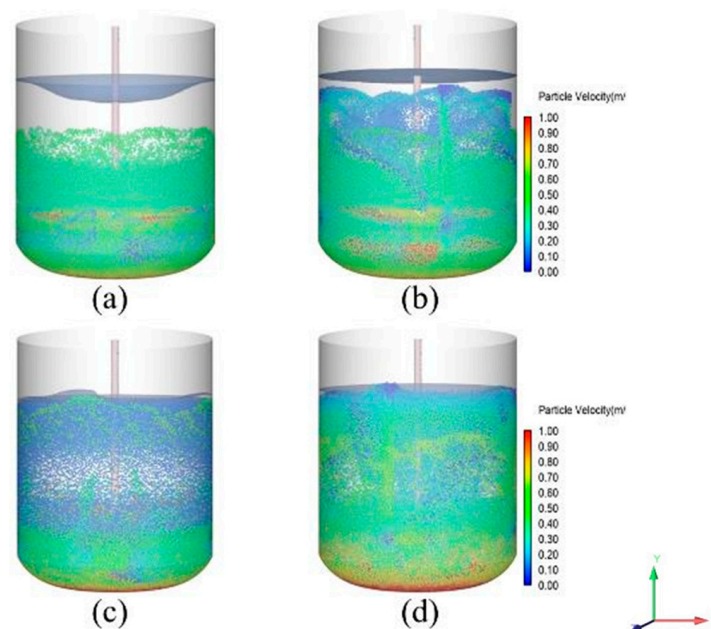
Figure 10. Snapshot of gas–liquid–solid flow with different impellers; (**a**) PBA30, (**b**) PBA45, (**c**) PBA60, and (**d**) Rushton.
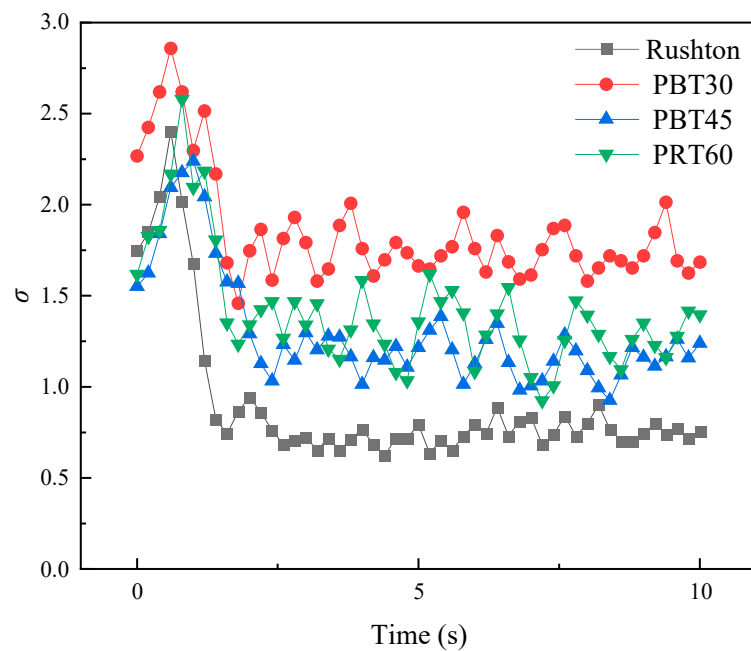
Figure 11. Time evolution of σ for different impellers.

Using this formula, the stirring torque under various conditions can be calculated by simulation for calculating the stirring power. The results are shown in Figure 12. The Rushton's power was the highest, and its power was almost four times that of PBA30. Meanwhile, with the increase in blade angle, the stirring power gradually increased, which indicates that, to increase the blade angle, a motor with higher power is needed to drive blade rotation.
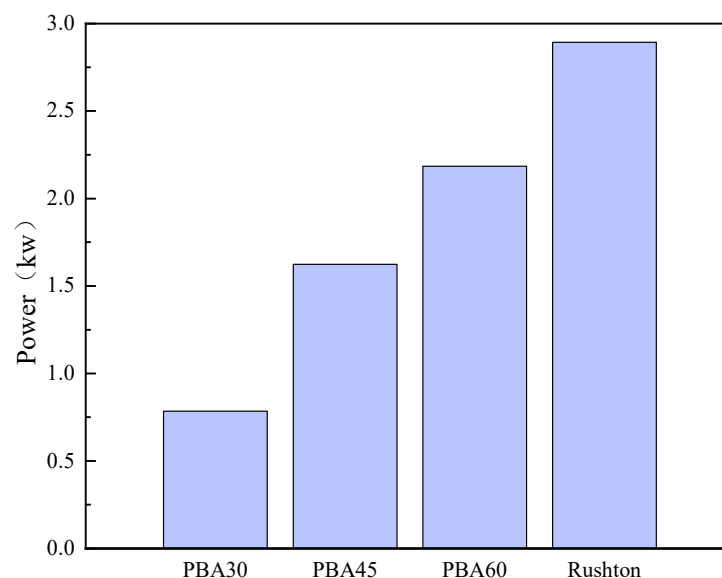

Figure 12. Influence of the impeller on power.

4.3.2. Effect of Mixing Tank Shape on Solid–Liquid Suspension

To improve the suspension performance, the shape of the bottom of the round-bottomed mixing tank needs to be optimized. In this study, blade type PBA45 was selected to optimize the height and width of the central bulge. The particle density was 2400 kg/m^3 and the rotational speed was N = 700 rpm.

Firstly, five different widths were selected, i.e., 0.02 m, 0.03 m, 0.04 m, 0.05 m, and 0.07 m. As shown in Figure 13a, the σ value changed more significantly when the width of the bulge was 0.02 m or 0.03 m, and the σ value changed slowly when the bulge width exceeded 0.04 m, at which point changing the bulge width did not have a significant effect on particle suspension. The σ values at 0.05 m and 0.07 m were almost identical.
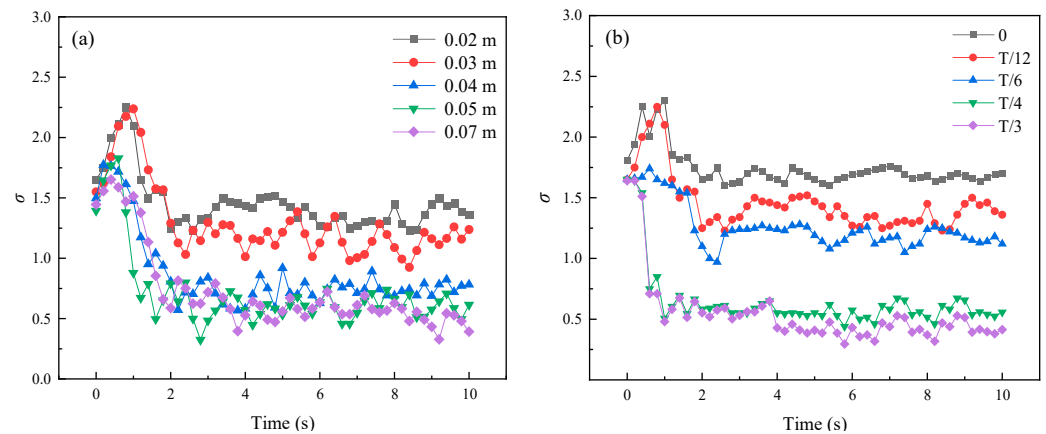

Figure 13. Evolution of σ over time; (**a**) different widths, (**b**) different heights.

Secondly, five different projection heights were selected for this study, i.e., D = 0, T/12, T/6, T/4, and T/3. For different optimized bottom structures, the time required for A to reach a steady state will be different. The σ values were calculated separately for different heights, as shown in Figure 13b, and the time to reach a steady state in the tank was greater than 5 s or longer for a raised height of 0, T/12, and only 2 s for the other three raised heights. The graph shows that the higher the bump height, the more homogeneous the mixing of the particles in the tank, and that the suspension of the particles in the tank increased significantly above T/12, but slowed down when the bump height increased to T/6. The study shows that the σ value was close to 0.5 when the bump height was T/4 or T/3, indicating that the suspension effect reached its optimum state.

It can be seen from the graph that changing the width of the projection did not improve the suspension effect as much as changing the height, and after increasing the height of the projection to a certain level, the particle suspension effect did not improve much. Therefore, in practical industrial applications, a relatively simple manufacturing process should be chosen to improve and optimize the mixing tank.

In addition to the effect of particle suspension uniformity on the leaching rate during vanadium shale leaching, increasing the number of particle collisions can also increase the leaching rate of vanadium. Bump widths of 0.05 m and 0.07 m, as well as bump heights of T/4 and T/3 were considered in this study. As shown in Figure 14, after the flow field stabilized, the number of particle collisions was stable at around 8200 for a width of 0.05 m and at around 7700 for a width of 0.07 m. When the height of the bulge was T/4, the number of collisions was stable at about 8000 times, while the number of collisions at T/3 was 7500 times. This shows that the lower the σ value, the higher the particle suspension, but at the same time, the number of particle collisions decreases, so a reasonable value should be chosen for the width and height of the raised surface of the bottom. The combination of the above analyses shows that the parameters of the surface base were most reasonable at a projection width of 0.05 m and height of T/4.
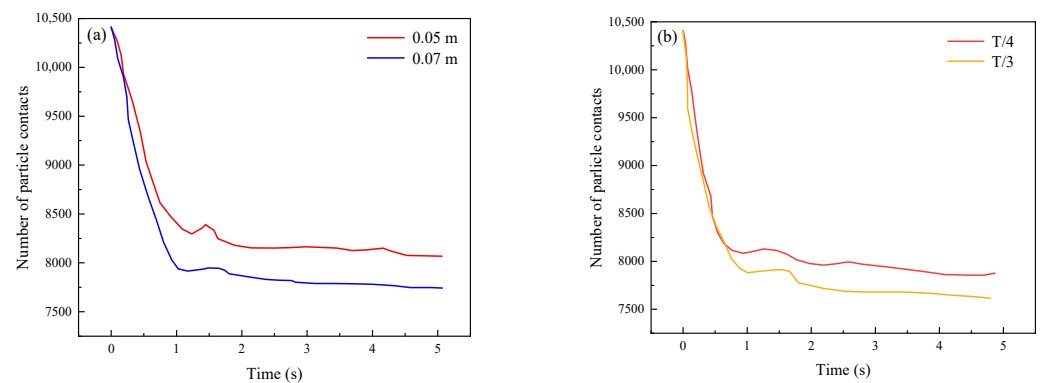
Figure 14. Number of particle contacts at (**a**) different widths and (**b**) different heights.

4.4. Validation of the Optimization of the Structure of the Mixing Tank

Based on the above research data, the optimal parameters of the circular bottom stirring tank were selected and the solid model was produced by 3D printing technology. Vanadium shale particles of 2–3 mm from Tongshan Mine in Hubei Province were selected to compare the speed of the flat-bottomed stirring tank with that of the round-bottomed stirring tank. As shown in Figure 15, at 300 rpm, some particles in the round-bottomed agitator were suspended in the upper part of the impeller, and the eddy current phenomenon was not obvious, while in the flat-bottomed agitator, particles were still in a critical suspension state. When the rotational speed increased to 400 rpm and 500 rpm, the particles in the round-bottomed mixing tank were already suspended in the upper part of the tank. At this time, the flat-bottomed mixing tank produced more eddy currents, and the particles were not highly suspended, which was the same as Figure 7a,b in the simulation. The particles were concentrated in the lower part of the tank. The experiment shows that the improved round-bottomed stirring tank could improve the suspension of particles.
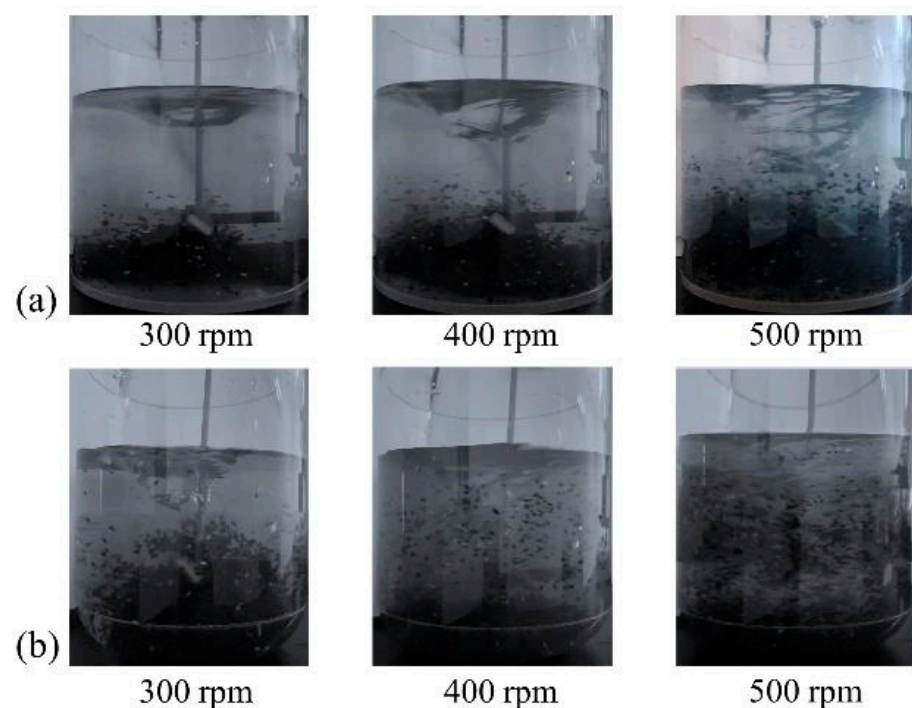
Figure 15. Mixing effects of two mixing tanks; (**a**) flat-bottomed agitator, (**b**) round-bottomed agitator.

5. Conclusions

In this study, the solid–liquid mixing process in stirring tanks of different shapes was investigated using the DEM-VOF method and the mixing effect of particles was analyzed from the point of view of spatial distribution. Structural optimization of the bottom shape of conventional stirring tanks was carried out and advice is provided for the choice of impeller type. The research in this paper is summarized as follows:

1. The uniformity of particle suspension was related to the height of the structure at the bottom of the mixing tank. The sudden change in velocity of the flow field at the bottom of a flat-bottomed stirring tank led to the stratification of the particles when the particle density was low, while the flow field at the bottom of the round-bottomed stirring tank formed a circular flow, which alleviated the sudden change in velocity at the bottom and suppressed the stratification of the particles.

2. The inclination of the paddle had a great influence on particle suspension and homogeneity, and PBA45 had the best mixing effect as the inclined blade paddle. At the same time, it was found that the mixing effect of the Rushton was better than that of the inclined blade paddle, but the power of the Rushton was greater, about two times higher than that of the PBA45, and its economic applicability should be considered in industrial production.

3. The suspension of the particles was closely related to the shape of the mixing tank. In this study, the structure of the stirring tank was optimized for particles with a density of 2400 kg/m^3 at different bulge widths and heights. The number of particle collisions should be considered to obtain the highest leaching rate when the difference in suspension uniformity is not too great. The optimum structure parameters were finally determined to be 0.05 m in width and T/4 in height, providing a good guide for industrial production and the optimization of the stirred tank structure.

Author Contributions: Y.H.: Conceptualization, Methodology, Investigation, Data Curation, Writing—Original Draft, Writing—Review and Editing. N.X.: Validation, Writing—Review and Editing, Supervision, Funding acquisition. Y.Z.: Resources, Validation, Writing—Review and Editing, Supervision, Funding acquisition. Q.Z.: Validation, Writing—Review and Editing, Supervision, Project administration. All authors have read and agreed to the published version of the manuscript.

Data Availability Statement: Not applicable.

Conflicts of Interest: We have no known competing financial interests or personal relationships that could have appeared to influence the work reported in this paper.

References

1. Paul, E.L.; Atiemo-Obeng, V.A.; Kresta, S.M. *Handbook of Industrial Mixing: Science and Practice*; John Wiley & Sons: Hoboken, NJ, USA, 2004.
2. Kresta, S.M.; Etchells, A.W., III; Dickey, D.S.; Atiemo-Obeng, V.A. *Advances in Industrial Mixing: A Companion to the Handbook of Industrial Mixing*; John Wiley & Sons: Hoboken, NJ, USA, 2015.
3. Nienow, A.W.; Edwards, M.F.; Harnby, N. *Mixing in the Process Industries*; Butterworth-Heinemann: Oxford, UK, 1997.
4. Visscher, F.; Van der Schaaf, J.; Nijhuis, T.; Schouten, J. Rotating Reactors-a Review. *Chem. Eng. Res. Des.* **2013**, *91*, 1923–1940. [CrossRef]
5. Tamburini, A.; Cipollina, A.; Micale, G.; Brucato, A.; Ciofalo, M. CFD Simulations of Dense Solid-Liquid Suspensions in Baffled Stirred Tanks: Prediction of Suspension Curves. *Chem. Eng. J.* **2011**, *178*, 324–341. [CrossRef]
6. Blais, B.; Bertrand, O.; Fradette, L.; Bertrand, F. CFD-DEM Simulations of Early Turbulent Solid-Liquid Mixing: Prediction of Sus-pension Curve and Just-Suspended Speed. *Chem. Eng. Res. Des.* **2017**, *123*, 388–406. [CrossRef]

7. Tamburini, A.; Cipollina, A.; Micale, G.; Brucato, A.; Ciofalo, M. CFD simulations of dense solid-liquid suspensions in baffled stirred tanks: Prediction of solid particle distribution. *Chem. Eng. J.* **2013**, *223*, 875–890. [CrossRef]
8. Scully, J.; Frawley, P. Computational Fluid Dynamics Analysis of the Suspension of Nonspherical Particles in a Stirred Tank. *Ind. Eng. Chem. Res.* **2011**, *50*, 2331–2342. [CrossRef]
9. Fan, Y.; Sun, J.; Jin, J.; Zhang, H.; Chen, W. The Effect of Baffle on Flow Structures and Dynamics Stirred by Pitch Blade Turbine. *Chem. Eng. Res. Des.* **2021**, *168*, 227–238. [CrossRef]
10. Shao, T.; Hu, Y.; Wang, W.; Jin, Y.; Cheng, Y. Simulation of Solid Suspension in a Stirred Tank Using CFD-DEM Coupled Approach. *Chin. J. Chem. Eng.* **2013**, *21*, 1069–1081. [CrossRef]
11. Hoseini, S.S.; Najafi, G.; Ghobadian, B.; Akbarzadeh, A.H. Impeller Shape-Optimization of Stirred-Tank Reactor: CFD and Fluid Structure Interaction Analyses. *Chem. Eng. J.* **2021**, *413*, 1–18. [CrossRef]
12. Tamburini, A.; Gagliano, G.; Micale, G.; Brucato, A.; Scargiali, F.; Ciofalo, M. Direct Numerical Simulations of Creeping to Early Turbulent Flow in Unbaffled and Baffled Stirred Tanks. *Chem. Eng. Sci.* **2018**, *192*, 161–175. [CrossRef]
13. Gonzalez-Neria, I.; Alonzo-Garcia, A.; Martínez-Delgadillo, S.A.; Mendoza-Escamilla, V.X.; Yanez-Varela, J.A.; Verdin, P.G.; Rivadeneyra-Romero, G. PIV and Dynamic LES of the Turbulent Stream and Mixing Induced by a V-Grooved Blade Axial Agitator. *Chem Eng. J.* **2019**, *374*, 1138–1152. [CrossRef]
14. Saikali, E.; Rodil, M.G.; Bois, G.; Bieder, U.; Leterrier, N.; Bertrand, M.; Dolias, Y. Validation of the Hydrodynamics in a Turbulent Un-Baffled Stirred Tank: A Necessity for Vortex-Reactor Precipitation Studies. *Chem. Eng. Sci.* **2020**, *214*, 1–19.
15. Zhang, W.; Chen, X.; Pan, W.; Xu, J. Numerical Simulation of Wake Structure and Particle Entrainment Behavior during a Single Bubble Ascent in Liquid-Solid System. *Chem. Eng. Sci.* **2022**, *253*, 117573. [CrossRef]
16. Zhang, L.; Feng, Z.; Sun, M.; Guan, H.; Jin, H.; Shi, H. Modeling of Long-Term Shock Interaction with a Movable Particle Curtain in a Rectangular Tube Based on a Dense Discrete Phase Model. *Powder Technol.* **2023**, *415*, 118116. [CrossRef]
17. Xu, L.; Wu, F.; Wang, J. DDPM Simulation of the Erosion of Immersed Tubes in a Pulsating Fluidized Bed. *Chem. Eng. Sci.* **2023**, *269*, 118475. [CrossRef]
18. Derksen, J.J. Numerical Simulation of Solids Suspension in a Stirred Tank. *Am. Inst. Chem. Eng.* **2003**, *49*, 2700–2714. [CrossRef]
19. Grenville, R.; Mak, A.; Brown, D. Suspension of Solid Particles in Vessels Agitated by Axial Flow Impellers. *Chem. Eng. Res. Des.* **2015**, *100*, 282–291. [CrossRef]
20. Blais, B.; Lassaigne, M.; Goniva, C.; Fradette, L.; Bertrand, F. Development of an Unresolved CFD-DEM Model for the Flow of Viscous Suspensions and its Application to Solid–Liquid Mixing. *J. Comput. Phys.* **2016**, *318*, 201–221. [CrossRef]
21. Satjaritanun, P.; Regalbuto, J.R.; Regalbuto, J.A. Mixing Optimization with Inward Flow Configuration Contra-Rotating Impeller, Baffle-Free Tank. *Alex. Eng. J.* **2021**, *60*, 3759–3779. [CrossRef]
22. Woziwodzki, S.; Broniarz-Press, L.; Ochowiak, M. Effect of Eccentricity on Transitional Mixing in Vessel Equipped with Turbine Impellers. *Chem. Eng. Res. Des.* **2010**, *88*, 1607–1614. [CrossRef]
23. Ameur, H. Effect of the Shaft Eccentricity and Rotational Direction on the Mixing Characteristics in Cylindrical Tank Reactors. *Chin. J. Chem. Eng.* **2016**, *24*, 1647–1654. [CrossRef]
24. Wu, L.; Gong, M.; Wang, J. Development of a DEM-VOF Model for the Turbulent Freesurface Flows with Particles and its Application to Stirred Mixing System. *Ind. Eng. Chem. Res.* **2018**, *57*, 1714–1725. [CrossRef]
25. Kang, Q.; He, D.; Zhao, N.; Feng, X.; Wang, J. Hydrodynamics in Unbaffled Liquid-Solid Stirred Tanks with Free Surface Studied by DEM-VOF Method. *Chem. Eng. J.* **2020**, *386*, 122846. [CrossRef]
26. Jia, H.; Wang, F.; Wu, J.; Tan, X.; Li, M. CFD Research on the Influence of 45° Disk Turbine Agitator Blade Diameter on the Solid–Liquid Mixing Characteristics of the Cone-Bottom Stirred Tank. *Arab. J. Sci. Eng.* **2020**, *45*, 5741–5749. [CrossRef]
27. Wu, T.R.; Chu, C.R.; Huang, C.J.; Wang, C.Y.; Chien, S.Y.; Chen, M.Z. A Two-Way Coupled Simulation of Moving Solids in Free-Surface Flows. *Comput. Fluids* **2014**, *100*, 347–355. [CrossRef]
28. ANSYS, Inc. *ANSYS FLUENT Theory Guide, Release 15*; ANYSYS: Canonsburg, PA, USA, 2013.
29. Ferziger, J.H.; Peric, M. *Computational Methods for Fluid Dynamics*, 3rd ed.; Springer: Berlin/Heidelberg, Germany, 2002.
30. Derakhshani, S.M.; Schott, D.L.; Lodewijks, G. Micro–Macro Properties of Quartz Sand: Experimental Investigation and DEM Simulation. *Powder Technol.* **2015**, *296*, 127–138. [CrossRef]
31. Bohnet, M.; Niesmak, G. Distribution of Solids in Stirred Suspensions. *Ger. Chem. Eng.* **1980**, *3*, 57–65.
32. Xie, L.; Luo, Z.H. Modeling and Simulation of the Influences of Particle-Particle Interactions on Dense Solid-Liquid Suspensions in Stirred Vessels. *Chem. Eng. Sci.* **2018**, *176*, 439–453. [CrossRef]